

Learning from the Right Patches: A Two-Stage Wavelet-Driven Masked Autoencoder for Histopathology Representation Learning

Raneen Younis

PLRI Medical Informatics Institute
CAIMed Reserch Center
Hannover Medical School

Younis.Raneen@mh-hannover.de

Lukas Chavez

Sanford Burnham Prebys Medical Discovery Institute
Rady Children’s Institute for Genomic Medicine
University of California San Diego

lchavez@sbpdiscovery.org

Louay Hamdi

Computer Science Institute
Leibniz University Hannover

louay.hamdi@stud.uni-hannover.de

Zahra Ahmadi

PLRI Medical Informatics Institute
CAIMed Reserch Center
Hannover Medical School

Ahmadi.Zahra@mh-hannover.de

Abstract

Whole-slide images are central to digital pathology, yet their extreme size and scarce annotations make self-supervised learning essential. Masked Autoencoders (MAEs) with Vision Transformer backbones have recently shown strong potential for histopathology representation learning. However, conventional random patch sampling during MAE pretraining often includes irrelevant or noisy regions, limiting the model’s ability to capture meaningful tissue patterns. In this paper, we present , a lightweight and domain-adapted framework that brings structure and biological relevance into MAE-based learning through a wavelet-informed patch selection strategy. WISE-MAE applies a two-step coarse-to-fine process: wavelet-based screening at low magnification to locate structurally rich regions, followed by high-resolution extraction for detailed modeling. This approach mirrors the diagnostic workflow of pathologists and improves the quality of learned representations. Evaluations across multiple cancer datasets, including lung, renal, and colorectal tissues, show that WISE-MAE achieves competitive representation quality and downstream classification performance while maintaining efficiency under weak supervision.

1. Introduction

Histopathology remains one of the most essential tools in cancer diagnosis, providing fine-grained insight into tissue morphology that directly influences clinical decision-making. With the transition from glass slides to digitized

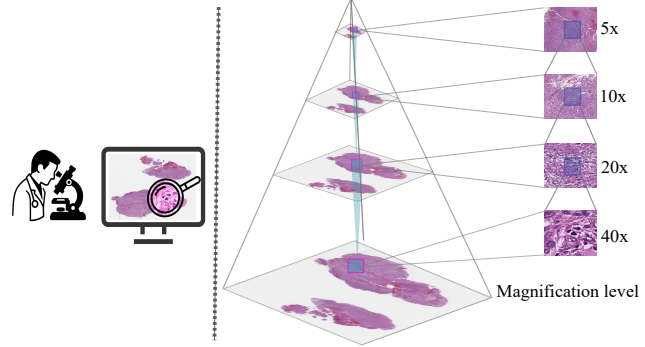


Figure 1. Illustration of hierarchical analysis in computational pathology. Left: A pathologist examines a whole-slide image and zooms into regions of diagnostic interest, a process mimicked in computational models. Right: Multi-resolution representation of the same WSI across magnification levels. Lower layers correspond to higher magnification with finer tissue detail, reflecting the increasing structural information accessed through zooming.

whole-slide images (WSIs), computational pathology has emerged as a powerful area for applying machine learning to histological analysis. WSIs capture vast amounts of visual information—often exceeding 100,000 pixels per dimension—making them rich in diagnostic content but also computationally challenging to process. To manage this complexity, most approaches divide WSIs into smaller image patches, often using the Multiple Instance Learning (MIL) framework [9], where a slide is treated as a bag of patches. While MIL methods have demonstrated strong performance in WSI classification, they face several limita-

tions in practice. First, not all extracted patches contribute equally to the diagnostic task. Random sampling often captures large portions of background, fat, or benign tissue [10, 12], which reduces the overall effectiveness of downstream task learning. In addition, many MIL-based models assume independence among patches [16, 40], thereby ignoring the spatial and morphological continuity that exists across tissue structures. To address this, recent approaches have adopted transformers to model inter-patch dependencies more effectively [27]. However, a more fundamental challenge persists: the sparsity of relevant diagnostic regions. Tumor prevalence within whole-slide images varies significantly across tasks. In some cases, tumor regions occupy only a small fraction of the slide (e.g., metastasis detection), making informative patch identification challenging, whereas in others (e.g., primary tumor slides), tumor coverage is more extensive. Without explicit guidance, random sampling often includes background or benign regions, diluting the model’s focus on diagnostically relevant features.

Recent advances in self-supervised learning (SSL) have opened new possibilities for medical imaging, where labeled data is often limited. In particular, masked image modeling (MIM) techniques such as masked autoencoders [34] have shown strong potential by learning to reconstruct hidden parts of images without requiring manual annotations. Compared to contrastive learning [18, 26], MAEs offer a more computationally friendly training pipeline, free from the need for large batch sizes or carefully curated positive/negative pairs, making them especially suitable for pathology, where access to GPUs and annotated data is often constrained [4, 13]. However, the effectiveness of MAEs in histopathology still depends on the quality of the patches used during training. Many existing approaches rely on random patch sampling, which can overwhelm the model with irrelevant or low-content regions [10, 24]. Moreover, most foundational models assume access to huge datasets and high computational budgets, which are not always feasible in real-world clinical settings.

To address these challenges, we propose Wavelet-Informed Sampling for Encoding Masked AutoEncoder (WISE-MAE), a lightweight, two-stage self-supervised framework tailored for histopathology. The design of WISE-MAE is inspired by how pathologists navigate WSIs, as illustrated in Figure 1. Typically, a pathologist first scans the slide at low magnification to locate suspicious regions and then zooms in to inspect fine-grained tissue details. Mimicking this diagnostic process, our method first performs wavelet-based frequency analysis at low resolution to identify the most informative tissue areas. From these selected regions, we extract high-resolution patches and apply masked autoencoding to encourage the model to learn both detailed intra-patch features and broader contextual pat-

terns. This two-stage training strategy allows WISE-MAE to maximize data efficiency while remaining computationally lightweight, making it practical for setups with limited hardware resources. Our approach aligns naturally with the hierarchical and multi-scale structure of tissue morphology and supports efficient pretraining under weak supervision using only slide-level labels. In summary, our main contributions are as follows:

- **Wavelet-guided Multi-resolution Patch Selection:** We propose a biologically inspired patch selection strategy that mimics the workflow of pathologists. Specifically, we use wavelet-based frequency scoring at intermediate resolution to identify structurally rich tissue regions, from which high-resolution patches are extracted for downstream processing. This component constitutes the core novelty of our framework and provides a principled way to guide representation learning toward biologically meaningful content.
- **MAE Adaptation for Histopathology:** We adapt existing Vision Transformer-based Masked Autoencoder (ViT-MAE) frameworks to histopathology by integrating our proposed sampling strategy, enabling the model to learn meaningful representations from high-resolution tissue patches in a self-supervised manner.
- **Label-efficient Focus on Informative Regions:** By combining wavelet-based scoring with multi-resolution patch selection, our method guides the model’s attention toward diagnostically relevant areas of WSIs, without the need for pixel-level labels. This makes our framework especially suitable for weakly supervised and resource-constrained settings.
- **Comprehensive Empirical Evaluation:** We evaluate WISE-MAE on multiple downstream classification tasks using Camelyon16 [1], TCGA-RCC, and TCGA-NSCLC [31] datasets. Experimental results demonstrate that our approach consistently outperforms baseline methods and achieves competitive performance.

2. Related Work

2.1. Multiple Instance Learning

Bag-level classification methods in computational pathology typically fall into two broad categories: bag-based and instance-based approaches. Bag-based methods attempt to train instance classifiers by assigning pseudo-labels to individual patches and then aggregating the predictions of the top- k instances to make a final slide-level (bag-level) prediction [3, 7, 14, 16, 37]. In contrast, instance-based methods focus on learning meaningful representations from individual instances (patches) and then aggregate these features to form a high-level bag representation, which is directly used to predict the slide label [15, 23, 27, 28, 40]. Empirical evidence suggests that instance-based methods of

ten outperform their bag-based counterparts in real-world histopathology tasks. One widely adopted instance-based method is attention-based multiple instance learning (AB-MIL) [15], which proposes computing attention weights for each instance using a trainable neural attention mechanism. TransMIL [27] takes a different approach by employing transformer [32] architectures to explicitly model interactions among instances in a bag, enabling it to capture spatial and contextual dependencies across a whole slide image. However, most MIL pipelines still rely on random patch sampling, potentially including large non-informative background regions that can harm learning performance.

2.2. Self-Supervised Learning in Pathology

Self-supervised learning (SSL) has become a promising approach for histopathology, enabling models to learn transferable representations from unlabeled whole-slide images [2, 8]. While contrastive methods have shown early success by adapting techniques from natural images [29, 41], their performance often depends on carefully crafted augmentations [25, 38, 39] or domain-specific pretext tasks [21]. However, the visual homogeneity of histology slides and reliance on cropped views can limit their generalization ability. Masked autoencoders (MAEs) [13], part of the Masked Image Modeling (MIM) paradigm, have recently emerged as a compelling alternative [35], offering a more efficient and augmentation-free training pipeline. While Global Contrast-Masked Autoencoders [24] apply masking at the WSI grid level to emphasize global contextual learning, our approach focuses on frequency-based patch selection to prioritize structurally informative regions before masked reconstruction.

2.3. Leveraging Multi-Resolution Information in Histopathology

Pathologists rely on multiple magnification levels when examining tissue, making multi-resolution analysis essential for WSI-based diagnosis [30, 42]. Prior studies typically either combine features from different resolutions [20] or treat them as separate inputs within the same bag [11]. Closest to our work is Hierarchical Attention-Guided Multiple Instance Learning (HAG-MIL) [36], which explores pyramidal masking across resolutions. Unlike these approaches, our method integrates multi-resolution information hierarchically by first identifying informative regions at low magnification via wavelet analysis, then focusing masked autoencoding on high-resolution patches, in a way that mirrors how pathologists examine slides.

2.4. Patch Sampling Strategies

Existing patch selection strategies can be broadly categorized into random, attention-guided, and clustering-based approaches. Random sampling is simple and scalable but

often captures low-content regions with limited diagnostic value. Attention-guided methods, such as those used in ABMIL [15], prioritize patches based on learned relevance scores, while clustering-based frameworks [6] promote diversity by selecting representative instances from feature-space groupings. Frequency-domain representations have also been explored to enhance masked image modeling, as in FreMIM [33], which incorporates Fourier features for medical image reconstruction. In contrast, our method leverages wavelet transforms that provide localized, multi-scale frequency decomposition, enabling biologically grounded and fully unsupervised patch selection. By quantifying wavelet energy, WISE-MAE focuses on structurally rich tissue regions, improving the efficiency of self-supervised pretraining on histopathology slides.

3. The WISE-MAE Framework

The WISE-MAE framework introduces a wavelet-guided two-stage sampling pipeline to enhance masked autoencoder pretraining for whole-slide image representation learning under weak supervision. The overall workflow, as illustrated in Figure 2, consists of four main stages: low-resolution patch sampling with wavelet scoring, high-resolution patch refinement, MAE-based self-supervised pre-training, and MIL-based downstream classification.

3.1. Stage 1: Low-Resolution Patch Sampling via Wavelet Energy

Given the extreme size of WSIs, we begin by extracting non-overlapping image patches at a coarse magnification level (e.g. 10x). These low-resolution patches serve as the first filter for content-aware sampling. To quantify morphological richness, we apply a single-level 2D Discrete Wavelet Transform (DWT) to each patch using the Daubechies basis. This decomposes the image into four subbands: LL (low-frequency approximation) and LH , HL , HH (high-frequency detail coefficients in horizontal, vertical, and diagonal directions). The wavelet energy is computed as the sum of squared coefficients from the high-frequency bands:

$$E(x) = \sum_{i,j} (LH(i,j)^2 + HL(i,j)^2 + HH(i,j)^2). \quad (1)$$

The wavelet energy criterion was chosen because high-frequency detail coefficients correspond to edge-rich and texture-dense regions, which typically represent diagnostically relevant morphological features such as cellular boundaries, nuclei clusters, and stromal textures. We rank all patches by their wavelet energy scores and retain the top $k\%$ (typically 20%) for further inspection.

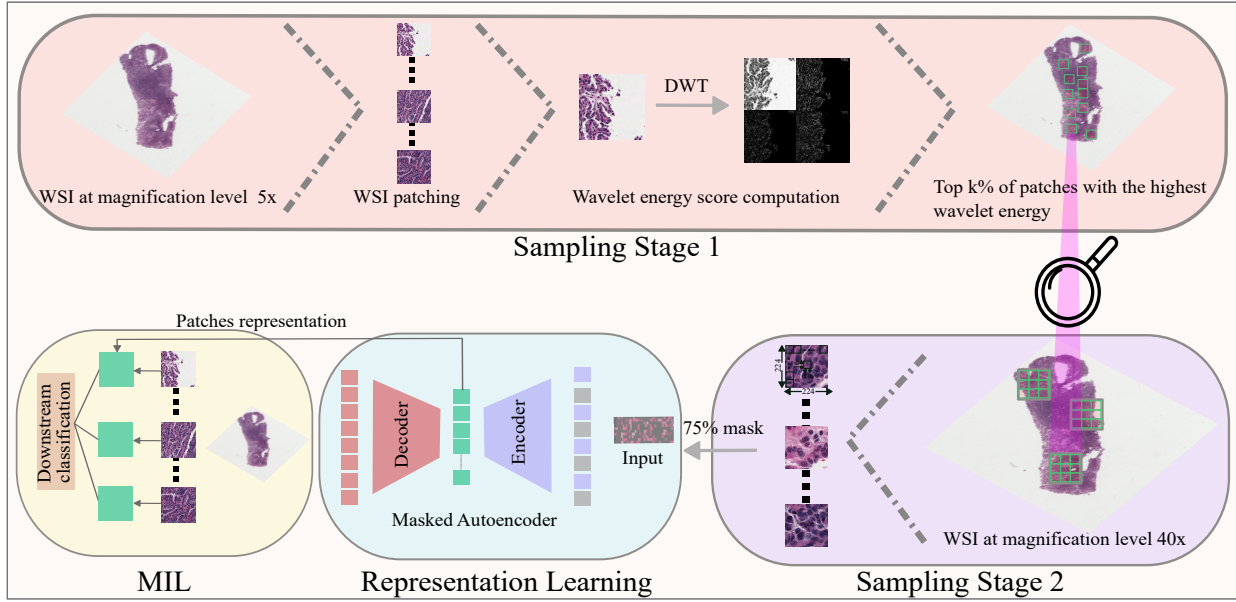


Figure 2. Overview of the WISE-MAE framework. The process begins with Stage 1 patch sampling at $5\times$ magnification (low resolution), where wavelet energy is computed for each patch to assess morphological richness. The top- $k\%$ patches with the highest energy scores are selected. In Stage 2, these selected regions are revisited at $40\times$ magnification (high resolution) to extract fine-grained patches containing rich tissue detail. These high-resolution patches are then used to train a Masked Autoencoder (MAE) in a self-supervised fashion. The learned encoder representations are subsequently used in an MIL framework for downstream classification tasks.

3.2. Stage 2: High-Resolution Patch Refinement

After identifying the top $k\%$ wavelet-rich regions from Stage 1, we proceed to extract the corresponding high-resolution patches at $40\times$ magnification using the original slide coordinates. This step captures more granular histological structures such as nuclei, mitotic figures, and glandular architecture, which are not visible at lower magnifications. Each selected low-resolution patch center is mapped back to its high-resolution coordinates, from which we extract a 224×224 pixel patch. Although wavelet energy is computed independently for each patch, the spatial topology of the WSI is preserved through coordinate indexing, ensuring that the transition from low- to high-resolution sampling maintains the original tissue layout.

This two-stage, coarse-to-fine pipeline avoids redundant sampling, focuses computational resources on informative tissue areas, and mimics the diagnostic approach of human pathologists, who zoom in on suspicious areas after initial low-magnification screening.

3.3. Self-Supervised MAE Pretraining

The final set of high-resolution patches is used to train a Masked Autoencoder (MAE) [13]. We adopt the MAE with a ViT-Base encoder, which provides a strong trade-off between representational power and training feasibility. Smaller ViT variants, such as ViT-Small or ViT-Tiny, often

lack the capacity to model the rich textural and spatial complexity of histopathology. In contrast, ViT-Base enables expressive learning while being computationally practical, as demonstrated in prior medical imaging benchmarks [5].

Encoder Design

The encoder f_{enc} follows the ViT-Base configuration with 12 transformer blocks, 12 attention heads, and a hidden embedding dimension of $D = 768$. Each input tile of size 224×224 is divided into $N = 196$ non-overlapping patches of size 16×16 . Each patch is flattened into a vector $x_i \in \mathbb{R}^P$, where $P = 16 \times 16 \times 3 = 768$, and linearly projected into the embedding space using:

$$z_i = W_e \cdot \text{flatten}(x_i) + p_i, \quad W_e \in \mathbb{R}^{D \times P}, \quad p_i \in \mathbb{R}^D. \quad (2)$$

We adopt the MAE masking strategy, where 75% of the patches are randomly masked and omitted from the encoder input. Only the visible subset $\mathbf{X}_{\text{vis}} \in \mathbb{R}^{V \times P}$, with $V = 49$, is processed by the encoder:

$$\mathbf{Z}_{\text{vis}} = f_{\text{enc}}(\mathbf{X}_{\text{vis}}) \in \mathbb{R}^{V \times D}. \quad (3)$$

This approach enforces learning from sparse context without direct access to masked content.

Decoder Design

The decoder f_{dec} is a lightweight transformer with 4 layers and an embedding dimension of 512. Encoder outputs are first projected to match this dimension through a linear layer. The decoder reconstructs pixel values for the masked patches using the encoded visible tokens, learnable mask tokens, and shared positional encodings for all $N = 196$ positions. Masked tokens are added only at this stage, consistent with the MAE formulation. Reconstruction is performed in RGB pixel space, and the decoder is discarded after pretraining.

This asymmetric encoder-decoder design promotes semantically meaningful encoder representations while maintaining computational efficiency. Note that “multi-resolution” in our framework refers to the hierarchical patch sampling stage, not to reconstruction, which operates at a single ($40\times$) scale.

Training Objective

The reconstruction objective is the mean squared error (MSE) between predicted and true pixel values of masked patches:

$$\mathcal{L}_{\text{MSE}} = \frac{1}{|M|} \sum_{i \in M} \|\hat{x}_i - x_i\|^2, \quad (4)$$

where M is the set of masked patch indices, \hat{x}_i is the predicted output, and x_i is the ground-truth pixel vector. This formulation ensures the encoder learns meaningful latent representations from incomplete visual contexts.

For the contrastive variant, an InfoNCE loss is incorporated to enhance representation discrimination:

$$\mathcal{L}_{\text{con}} = -\log \frac{\exp(\text{sim}(z_i, z_i^+)/\tau)}{\sum_{j=1}^N \exp(\text{sim}(z_i, z_j^-)/\tau)}, \quad (5)$$

where $\text{sim}(\cdot, \cdot)$ denotes cosine similarity and τ is the temperature parameter. The total objective combines both components as

$$\mathcal{L} = \mathcal{L}_{\text{MSE}} + \lambda \mathcal{L}_{\text{con}}. \quad (6)$$

After training, the decoder is removed, and the pretrained encoder is retained to extract patch-level embeddings for downstream tasks.

3.4. Downstream Classification via MIL

After self-supervised pretraining, the encoder is frozen and used to extract patch-level feature embeddings from high-resolution WSI tiles. These embeddings represent semantically rich tissue characteristics learned during masked autoencoding and serve as input for downstream classification tasks.

Under a weakly supervised multiple instance learning (MIL) paradigm, each whole-slide image is treated as a bag

of instance embeddings, with supervision provided only at the slide level. Various MIL architectures can be employed in this setting, including attention-based pooling [15].

In this work, we adopt an attention-based MIL formulation using the CLAM framework [23], which learns to assign soft importance weights to each patch and aggregates features via a gated attention mechanism. The final slide-level prediction is obtained through a fully connected layer applied to the weighted feature representation. During training, only the parameters of the aggregation and classification modules are updated, while the pretrained encoder remains fixed.

4. Experimental Analysis

4.1. Datasets and Metrics

We evaluate our approach using several publicly available whole-slide image datasets covering a range of organs and cancer types. All datasets provide slide-level labels, making them suitable for weakly supervised learning under a multiple instance learning (MIL) framework.

- **TCGA-NSCLC:** The Cancer Genome Atlas Non-Small Cell Lung Cancer (TCGA-NSCLC) dataset [31] comprises two major subtypes: lung adenocarcinoma (LUAD) and lung squamous cell carcinoma (LUSC). A total of 993 diagnostic WSIs were included, with 507 LUAD and 486 LUSC slides. Patch extraction at $40\times$ magnification results in approximately 9,958 patches per slide on average. The data is split into training, validation, and test sets using a 7:1:2 ratio.
- **TCGA-RCC:** The TCGA Renal Cell Carcinoma (TCGA-RCC) cohort [31] includes 884 WSIs from three renal cancer subtypes: clear cell (KIRC), papillary (KIRP), and chromophobe (KICH). The slides yield an average of 13,907 high-resolution patches at $40\times$ magnification. Data is divided into training, validation, and test subsets using the same 7:1:2 split.
- **CAMELYON16:** CAMELYON16 is a benchmark dataset [1] for lymph node metastasis detection in breast cancer. It contains 400 WSIs annotated with binary slide-level labels (metastatic vs. normal). All slides are scanned at $40\times$ magnification, reflecting realistic clinical variability in staining and preparation.

To assess model performance, we report three standard classification metrics: Accuracy (Acc), F1-score, and area under the ROC curve (AUC). These metrics provide a comprehensive view of both overall and class-specific prediction quality.

4.2. Implementation Details

For MAE pretraining, we use approximately 80% of slides from TCGA-NSCLC and TCGA-RCC, as well as CAMELYON16, which are selected to ensure diverse tissue cov-

Model	TCGA-NSCLC			TCGA-RCC			CAMELYON16		
	Acc	AUC	F1	Acc	AUC	F1	Acc	AUC	F1
Max Pooling	0.774	0.863	0.774	0.880	0.970	0.847	0.682	0.715	0.549
AB-MIL [15]	0.817	0.903	0.817	0.892	0.978	0.864	0.868	0.903	0.850
CLAM-SB [23]	0.824	0.905	0.824	0.878	0.970	0.846	0.819	0.834	0.782
CLAM-MB [23]	0.818	0.900	0.818	0.895	0.975	0.871	0.826	0.876	0.800
TransMIL [27]	0.825	0.902	0.825	0.876	0.972	0.850	0.809	0.838	0.787
DTFD-MIL [40]	0.838	0.902	0.830	0.898	0.976	0.884	0.899	0.933	0.858
MAE [13]	0.841	0.910	0.841	0.885	0.962	0.860	0.826	0.856	0.748
HAG-MIL [36]	0.849	0.921	0.849	0.914	0.982	0.894	0.887	0.946	0.874
DS-MIL [19]	0.888	0.939	0.876	0.929	0.984	0.890	0.856	0.899	0.815
DTFD-MIL [40]	0.824	0.887	0.823	0.962	0.991	0.962	0.897	0.945	0.864
GCMAE [24]	0.857	0.925	0.857	0.905	0.979	0.889	0.864	0.909	0.829
WiKG [22]	0.840	0.907	0.839	0.970	0.996	0.970	0.900	0.925	0.883
WISE-MAE	0.873	0.933	0.873	0.898	0.974	0.872	0.880	0.918	0.836
WISE-MAE+Contrastive	0.887	0.944	0.887	0.917	0.985	0.896	0.905	0.953	0.889

Table 1. Performance comparison across TCGA-NSCLC, TCGA-RCC, and CAMELYON16. Metrics include Acc, AUC, and F1-score. The best results for each dataset are highlighted in bold.

erage. Patches are sampled via wavelet-guided selection at $10\times$ and extracted at $40\times$ resolution. Pretraining is performed using ViT-Base with a patch size of 16×16 , embedding dimension 768, and 75% random masking. The model is trained for 300 epochs using AdamW with a learning rate of ($\text{lr} = 1 \times 10^{-4}$, weight decay of 0.05, and cosine decay schedule. For downstream evaluation, the remaining 20% of slides are used across binary and multiclass classification tasks. Patch embeddings are extracted from the frozen encoder and passed to a CLAM-based attention MIL classifier. All downstream models are trained with Adam ($\text{lr} = 2 \times 10^{-4}$, weight decay = 1×10^{-5}), batch size 1, and early stopping on validation loss. Features and metadata are stored in HDF5 format. All experiments are run on 4 NVIDIA H100 GPUs using PyTorch.

4.3. Comparison with State-of-the-arts

We compare the performance of WISE-MAE with state-of-the-art MIL and self-supervised frameworks on the TCGA-NSCLC, TCGA-RCC, and CAMELYON16 datasets (Table 1). Unlike most existing WSI classification methods, WISE-MAE is engineered for efficiency, containing approximately 100K trainable parameters—substantially fewer than typical attention-based MIL models, which are reported to have between 0.8M and 1.2M parameters in recent MIL benchmarks [17].

Most existing MIL approaches rely on either random or attention-driven patch sampling. For example, Max Pooling and MAE [13] employ random sampling without prioritization, whereas ABMIL [15], CLAM [23], TransMIL [27], and DS-MIL [19] utilize learned attention mechanisms to

identify diagnostically relevant regions. Clustering-based methods such as CLAM-SB [23] and DTFD-MIL [40] further increase complexity by combining attention pooling with instance-level clustering. GCMAE [24] enhances MAE pretraining through global context modeling but still depends on random patch selection.

In contrast, WISE-MAE introduces a biologically motivated, fully unsupervised wavelet-guided patch selection strategy that prioritizes structurally informative tissue regions before pretraining, thereby reducing redundancy and enhancing data utilization. Despite its compact architecture, WISE-MAE achieves comparable or superior results on two of the three benchmark datasets (TCGA-NSCLC and CAMELYON16), demonstrating that targeted patch selection can deliver competitive performance even with a lightweight model. Furthermore, the contrastive variant of WISE-MAE improves discriminative capability without increasing model depth or parameter count.

4.4. Generalizability of WISE-MAE

To evaluate the generalization capability of WISE-MAE, we conducted three transfer experiments spanning inter-organ, cross-domain, and cross-task settings: (i) colorectal tissue classification after pretraining on lung cancer slides, (ii) lung cancer subtyping after pretraining on renal cancer, and (iii) metastasis detection after pretraining on renal cancer.

TCGA-NSCLC → NCT-CRC: This setting assesses robustness to significant tissue type and staining variations. As shown in Table 3, WISE-MAE and its contrastive variant consistently outperform ViT and ResNet baselines, in-

Model	Acc	AUC	F1
Random ViT-B/16	0.684	0.742	0.660
ImageNet ViT-B/16	0.736	0.790	0.710
Random ResNet50	0.702	0.768	0.690
ImageNet ResNet50	0.751	0.825	0.730
MAE	0.876	0.931	0.880
GCMAE	0.891	0.945	0.890
WISE-MAE	0.908	0.962	0.910
WISE-MAE + Contrastive	0.923	0.972	0.930

Table 2. Cross-Task Transfer from TCGA-RCC (Renal Cancer) to CAMELYON16 (Lymph Node Metastasis Detection). Evaluation of generalization performance across WISE-MAE and baseline methods under organ and diagnostic domain shift.

cluding both random and ImageNet-initialized versions. While standard MAE and GCMAE models already show notable improvements over baselines, the WISE-MAE variants achieve further gains, with the contrastive version reaching the highest accuracy (0.937) and AUC (0.979). These results highlight the benefit of spatially aware, multi-resolution patch selection, and demonstrate that the contrastive objective strengthens representation consistency across tissue domains, enhancing transferability across tissue types.

TCGA-RCC → TCGA-NSCLC: This experiment tests cross-organ generalization by transferring from renal cancer classification to lung cancer subtyping. As shown in Table 4, WISE-MAE and its contrastive variant outperform all baseline models, including both random and ImageNet-initialized ResNet50 and ViT architectures. While MAE already provides a strong baseline, WISE-MAE achieves notable improvements in AUC (0.982 vs. 0.961) and F1-score (0.940 vs. 0.910), confirming the benefit of structured patch selection. The contrastive variant further boosts performance across all metrics, indicating that the contrastive objective contributes to more transferable and discriminative feature representations across organ types.

TCGA-RCC → CAMELYON16: This task represents a more difficult transfer setting involving both organ and diagnostic domain shift—from renal cancer classification to lymph node metastasis detection. As reported in Table 2, WISE-MAE again achieves strong results, outperforming MAE, GCMAE, and traditional supervised baselines across all metrics. The contrastive WISE-MAE variant yields the highest AUC (0.972) and F1-score (0.930), indicating its robustness and improved feature generalization under substantial cross-task and cross-domain shifts.

The improved transferability of WISE-MAE can be attributed to its focus on morphology-driven rather than appearance-based representations. The wavelet-guided sampling emphasizes patches with rich structural and tex-

Model	Acc	AUC	F1
Random ViT-B/16	0.721	0.788	0.700
ImageNet ViT-B/16	0.774	0.842	0.760
Random ResNet50	0.741	0.812	0.730
ImageNet ResNet50	0.793	0.861	0.780
MAE	0.868	0.935	0.870
GCMAE	0.881	0.951	0.890
WISE-MAE	0.906	0.961	0.900
WISE-MAE + Contrastive	0.937	0.979	0.930

Table 3. Cross-Domain Transfer from TCGA-NSCLC (Lung Cancer) to NCT-CRC (Colorectal Tissue Classification). Evaluation of WISE-MAE and its contrastive variant under substantial tissue type and staining variations.

Model	Acc	AUC	F1
Random ViT-B/16	0.762	0.893	0.770
ImageNet ViT-B/16	0.825	0.918	0.810
Random ResNet50	0.864	0.947	0.850
ImageNet ResNet50	0.886	0.961	0.870
MAE	0.891	0.933	0.910
WISE-MAE	0.910	0.979	0.930
WISE-MAE + Contrastive	0.926	0.982	0.940

Table 4. Cross-Organ Transfer from TCGA-RCC (Renal Cancer) to TCGA-NSCLC (Lung Cancer Subtyping). Performance comparison of WISE-MAE and baseline methods, highlighting improvements in AUC and F1 through structured patch selection and contrastive pretraining.

tural content, encouraging the encoder to learn features related to histological organization rather than stain or color variations. Since such morphological cues tend to remain stable across organs and datasets, the learned representations exhibit better generalization.

4.5. Ablation Studies

To understand the design choices that contribute to the effectiveness of WISE-MAE, we conducted a series of ablation studies. These include evaluations of wavelet family selection, masking ratios during pretraining, and the magnification strategy used for hierarchical patch selection. Each experiment is isolated and measured on downstream performance using the TCGA-NSCLC LUAD vs. LUSC classification task.

4.6. Wavelet Family Selection

Our patch selection strategy relies on high-frequency energy from wavelet subbands to guide the sampling of informative regions. The choice of wavelet family influences both the structural fidelity of selected patches and the efficiency of preprocessing. We evaluated three

Wavelet	Linear Probing		Fine-tuning	
	Acc	AUC	Acc	AUC
Haar	0.810	0.866	0.892	0.938
Daubechies (db4)	0.834	0.881	0.901	0.945
Symlets (sym5)	0.825	0.873	0.896	0.941

Table 5. Downstream classification performance on TCGA-NSCLC using different wavelet families for patch selection.

Mask Ratio	Linear Probing		CLAM-SB	
	Acc	AUC	Acc	AUC
60%	0.841	0.913	0.897	0.942
70%	0.850	0.920	0.899	0.944
75%	0.854	0.917	0.904	0.946
80%	0.832	0.905	0.896	0.937
90%	0.810	0.886	0.881	0.925

Table 6. Effect of masking ratio on downstream classification performance using WISE-MAE on TCGA-NSCLC.

standard wavelets—Haar, Daubechies (db4), and Symlets (sym5)—using MAE pretraining followed by classification via linear probing and fine-tuning. Daubechies (db4) consistently outperformed other families (see Table 5) in both evaluation settings. Its smoother basis functions likely enhance the ability to highlight morphological features such as gland boundaries and cellular textures relevant to lung cancer subtyping.

4.7. Masking Ratio Selection

The mask ratio in masked autoencoding influences how much of the image is hidden during pretraining. While a 75% ratio is standard in natural images, histopathology exhibits denser and more complex spatial features. We trained five MAE models on TCGA-NSCLC using different masking ratios (60%–90%) and evaluated both linear probing and downstream fine-tuning. Although linear probing peaked slightly at 70%, downstream performance favored 75%, indicating an optimal trade-off between pretext difficulty and feature quality (see Table 6). We therefore adopt 75% as our default mask ratio in all subsequent experiments.

4.8. Magnification Strategy Evaluation

To emulate clinical workflows, we employed a hierarchical patch selection scheme. Initial patch selection was performed at a medium magnification level, followed by high-resolution refinement. We compared three base magnifications ($5\times$, $10\times$, and $20\times$) for identifying candidate regions, with final patches consistently extracted at $40\times$. As summarized in Table 7, $10\times$ magnification produced the best

Base Magnification	Acc	AUC
$5\times$	0.872	0.932
$10\times$	0.904	0.946
$20\times$	0.893	0.939

Table 7. Impact of base magnification level on two-stage WISE-MAE performance on TCGA-NSCLC. High-resolution patches were consistently sampled at $40\times$.

Sampling Strategy	Acc	AUC
Multi-resolution ($10\times \rightarrow 40\times$)	0.884	0.932
Direct at $40\times$	0.839	0.894

Table 8. Comparison of classification performance with and without hierarchical sampling on TCGA-NSCLC.

results across all performance metrics. In contrast, $5\times$ often missed important spatial cues, while $20\times$ added computational overhead with marginal performance improvements. These results support the effectiveness of a coarse-to-fine strategy for balancing contextual awareness and cellular resolution.

4.9. Effect of Multi-resolution Sampling

To assess the contribution of hierarchical patch selection in WISE-MAE, we compared it to a simplified variant where patches were sampled and wavelet-scored directly at $40\times$, omitting the coarse-level screening at lower magnifications. As shown in Table 8, the multi-resolution ($10\times \rightarrow 40\times$) approach outperforms the single-scale variant, achieving higher accuracy (0.884 vs. 0.839) and AUC (0.932 vs. 0.894). This confirms the value of coarse-to-fine selection, which enables more informed patch choice by leveraging global tissue context.

In WISE-MAE, the $10\times$ magnification is used only during the patch sampling stage for wavelet-based analysis to identify regions rich in structural information. The self-supervised pretraining and downstream classification are performed exclusively on $40\times$ patches, which contain finer cellular details and more discriminative tissue features. Using $10\times$ solely for region selection thus ensures efficient sampling without compromising the high-resolution information necessary for model training. These results support the hypothesis that multi-resolution strategies, inspired by the diagnostic process of human pathologists, enhance self-supervised representation learning by prioritizing structurally informative regions early in the pipeline.

5. Conclusion

We introduced WISE-MAE, a masked autoencoder framework tailored to histopathology, combining wavelet-guided

patch sampling, multi-scale reconstruction, and optional contrastive learning. Our results demonstrate that domain-aware sampling significantly improves feature quality and transferability across datasets and diagnostic tasks. Multi-resolution learning further enhances the model’s ability to capture nested tissue structures, while contrastive objectives improve robustness to staining and domain shifts. Compared to standard MAE and existing baselines, WISE-MAE consistently yields stronger performance with greater parameter efficiency. While WISE-MAE shows strong generalization, limitations remain in terms of patch redundancy, domain-specific overfitting, and lack of end-to-end optimization. Future work will explore adaptive sampling and unified training strategies.

References

- [1] Babak Ehteshami Bejnordi, Mitko Veta, Paul Johannes Van Diest, Bram Van Ginneken, Nico Karssemeijer, Geert Litjens, Jeroen AWM Van Der Laak, Meyke Hermsen, Quirine F Manson, Maschenka Balkenhol, et al. Diagnostic assessment of deep learning algorithms for detection of lymph node metastases in women with breast cancer. *Jama*, 318(22):2199–2210, 2017. [2](#) [5](#)
- [2] Joseph Boyd, Mykola Liashuha, Eric Deutsch, Nikos Paragios, Stergios Christodoulidis, and Maria Vakalopoulou. Self-supervised representation learning using visual field expansion on digital pathology. In *Proceedings of the IEEE/CVF International Conference on Computer Vision*, pages 639–647, 2021. [3](#)
- [3] Gabriele Campanella, Michael G Hanna, Lisa Geneslaw, and et al. Clinical-grade computational pathology using weakly supervised deep learning on whole slide images. *Nature Medicine*, 25(8):1301–1309, 2019. [2](#)
- [4] Life Medical Centre. Histopathology and its vital role in diagnosing diseases. *Life Medical Centre Blog*, 2023. [2](#)
- [5] Richard J. Chen, Tong Ding, Ming Y. Lu, Drew F.K. Williamson, Guillaume Jaume, Andrew H. Song, Bowen Chen, Andrew Zhang, Daniel Shao, Muhammad Shaban, et al. Towards a general-purpose foundation model for computational pathology. *Nature Medicine*, 30(3):850–862, 2024. [4](#)
- [6] Wafa Chenni, Habib Herbi, Morteza Babaie, and Hamid R Tizhoosh. Patch clustering for representation of histopathology images. In *European Congress on Digital Pathology*, pages 28–37. Springer, 2019. [3](#)
- [7] Philip Chikontwe, Meejeong Kim, Soo Jeong Nam, Heounjeong Go, and Sang Hyun Park. Multiple instance learning with center embeddings for histopathology classification. In *International Conference on Medical Image Computing and Computer-Assisted Intervention*, pages 519–528. Springer, 2020. [2](#)
- [8] Alexander Chowdhury, Jacob Rosenthal, Jonathan Waring, and Renato Umeton. Applying self-supervised learning to medicine: review of the state of the art and medical implementations. In *Informatics*, page 59. MDPI, 2021. [3](#)
- [9] Alexey Dosovitskiy, Lucas Beyer, Alexander Kolesnikov, Dirk Weissenborn, Xiaohua Zhai, Thomas Unterthiner, Mostafa Dehghani, Matthias Minderer, Georg Heigold, Sylvain Gelly, Jakob Uszkoreit, and Neil Houlsby. An image is worth 16x16 words: Transformers for image recognition at scale. In *International Conference on Learning Representations (ICLR)*, 2021. [1](#)
- [10] Spyros Gidaris, Praveer Singh, and Nikos Komodakis. Unsupervised representation learning by predicting image rotations. In *International Conference on Learning Representations (ICLR)*, 2018. [2](#)
- [11] Noriaki Hashimoto, Daisuke Fukushima, Ryoichi Koga, Yusuke Takagi, Kaho Ko, Kei Kohno, Masato Nakaguro, Shigeo Nakamura, Hidekata Hontani, and Ichiro Takeuchi. Multi-scale domain-adversarial multiple-instance cnn for cancer subtype classification with unannotated histopathological images. In *Proceedings of the IEEE/CVF conference on computer vision and pattern recognition*, pages 3852–3861, 2020. [3](#)
- [12] Kaiming He, Haoqi Fan, Yuxin Wu, Saining Xie, and Ross Girshick. Momentum contrast for unsupervised visual representation learning. In *IEEE/CVF Conference on Computer Vision and Pattern Recognition (CVPR)*, pages 9729–9738, 2020. [2](#)
- [13] Kaiming He, Xinlei Chen, Saining Xie, Yanghao Li, Piotr Dollár, and Ross Girshick. Masked autoencoders are scalable vision learners. *Proceedings of the IEEE/CVF Conference on Computer Vision and Pattern Recognition (CVPR)*, pages 16000–16009, 2022. [2](#), [3](#), [4](#), [6](#)
- [14] Le Hou, Dimitris Samaras, Tahsin M Kurc, Yi Gao, James E Davis, and Joel H Saltz. Patch-based convolutional neural network for whole slide tissue image classification. In *Proceedings of the IEEE conference on computer vision and pattern recognition*, pages 2424–2433, 2016. [2](#)
- [15] Max Ilse, Jakub M Tomczak, and Max Welling. Attention-based deep multiple instance learning. In *Proceedings of the International Conference on Machine Learning (ICML)*, pages 2127–2136, 2018. [2](#), [3](#), [5](#), [6](#)
- [16] Fahdi Kanavati, Gouji Toyokawa, Seiya Momosaki, Michael Rambeau, Yuka Kozuma, Fumihiro Shoji, Koji Yamazaki, Sadanori Takeo, Osamu Iizuka, and Masayuki Tsuneki. Weakly-supervised learning for lung carcinoma classification using deep learning. *Scientific reports*, 10(1):9297, 2020. [2](#)
- [17] Hassan Keshvarikhojasteh, Josien Pluim, and Mitko Veta. Multi-head attention-based deep multiple instance learning. *arXiv preprint arXiv:2404.05362*, 2024. [6](#)
- [18] Daisuke Komura and Shumpei Ishikawa. Machine learning methods for histopathological image analysis. *Computational and Structural Biotechnology Journal*, 16:34–42, 2018. [2](#)
- [19] Bin Li, Yin Li, and Kevin W Eliceiri. Dual-stream multiple instance learning network for whole slide image classification with self-supervised contrastive learning. In *Proceedings of the IEEE/CVF conference on computer vision and pattern recognition*, pages 14318–14328, 2021. [6](#)
- [20] Jiayun Li, Wenyuan Li, Anthony Sisk, Huihui Ye, W Dean Wallace, William Speier, and Corey W Arnold. A multi-

resolution model for histopathology image classification and localization with multiple instance learning. *Computers in biology and medicine*, 131:104253, 2021. 3

[21] Jiajun Li, Tiancheng Lin, and Yi Xu. Sslp: Spatial guided self-supervised learning on pathological images. In *International conference on medical image computing and computer-assisted intervention*, pages 3–12. Springer, 2021. 3

[22] Jiawen Li, Yuxuan Chen, Hongbo Chu, Qiehe Sun, Tian Guan, Anjia Han, and Yonghong He. Dynamic graph representation with knowledge-aware attention for histopathology whole slide image analysis. In *Proceedings of the IEEE/CVF conference on computer vision and pattern recognition*, pages 11323–11332, 2024. 6

[23] Ming Y Lu, Drew FK Williamson, Tiffany Y Chen, Richard J Chen, Matteo Barbieri, and Faisal Mahmood. Data-efficient and weakly supervised computational pathology on whole-slide images. *Nature biomedical engineering*, 5(6):555–570, 2021. 2, 5, 6

[24] Hao Quan, Xingyu Li, Weixing Chen, Qun Bai, Mingchen Zou, Ruijie Yang, Tingting Zheng, Ruiqun Qi, Xinghua Gao, and Xiaoyu Cui. Global contrast-masked autoencoders are powerful pathological representation learners. *Pattern Recognition*, 156:110745, 2024. 2, 3, 6

[25] Colorado J Reed, Sean Metzger, Aravind Srinivas, Trevor Darrell, and Kurt Keutzer. Selfaugment: Automatic augmentation policies for self-supervised learning. In *Proceedings of the IEEE/CVF conference on computer vision and pattern recognition*, pages 2674–2683, 2021. 3

[26] Hrishikesh Sahasrabudhe, Azam Khan, and Nasir Rajaoot. Self-supervised magnification-agnostic histopathological feature learning. In *Medical Image Computing and Computer-Assisted Intervention (MICCAI)*, pages 535–544, 2020. 2

[27] Zhuchen Shao, Hao Bian, Yang Chen, Yifeng Wang, Jian Zhang, Xiangyang Ji, et al. Transmil: Transformer based correlated multiple instance learning for whole slide image classification. *Advances in neural information processing systems*, 34:2136–2147, 2021. 2, 3, 6

[28] Yash Sharma, Aman Shrivastava, Lubaina Ehsan, Christopher A Moskaluk, Sana Syed, and Donald Brown. Cluster-to-conquer: A framework for end-to-end multi-instance learning for whole slide image classification. In *Medical imaging with deep learning*, pages 682–698. PMLR, 2021. 2

[29] Saeed Shurab and Rehab Duwairi. Self-supervised learning methods and applications in medical imaging analysis: A survey. *PeerJ Computer Science*, 8:e1045, 2022. 3

[30] Hiroki Tokunaga, Yuki Teramoto, Akihiko Yoshizawa, and Ryoma Bise. Adaptive weighting multi-field-of-view cnn for semantic segmentation in pathology. In *Proceedings of the IEEE/CVF conference on computer vision and pattern recognition*, pages 12597–12606, 2019. 3

[31] Katarzyna Tomczak, Patrycja Czerwińska, and Maciej Wizerowicz. Review the cancer genome atlas (tcga): an immeasurable source of knowledge. *Contemporary Oncology/Współczesna Onkologia*, 2015(1):68–77, 2015. 2, 5

[32] Ashish Vaswani, Noam Shazeer, Niki Parmar, Jakob Uszkoreit, Llion Jones, Aidan N Gomez, Łukasz Kaiser, and Illia Polosukhin. Attention is all you need. In *Advances in Neural Information Processing Systems*. Curran Associates, Inc., 2017. 3

[33] Wenxuan Wang, Jing Wang, Chen Chen, Jianbo Jiao, Yuanxiu Cai, Shanshan Song, and Jiangyun Li. Fremim: Fourier transform meets masked image modeling for medical image segmentation. In *Proceedings of the IEEE/CVF winter conference on applications of computer vision*, pages 7860–7870, 2024. 3

[34] Xiyue Wang, Sen Yang, Jun Zhang, Minghui Wang, Jing Zhang, Wei Yang, Junzhou Huang, and Xiao Han. Transformer-based unsupervised contrastive learning for histopathological image classification. *Medical Image Analysis*, 81:102559, 2022. 2

[35] Chen Wei, Haoqi Fan, Saining Xie, Chao-Yuan Wu, Alan Yuille, and Christoph Feichtenhofer. Masked feature prediction for self-supervised visual pre-training. In *Proceedings of the IEEE/CVF conference on computer vision and pattern recognition*, pages 14668–14678, 2022. 3

[36] Conghao Xiong, Hao Chen, Joseph JY Sung, and Irwin King. Diagnose like a pathologist: transformer-enabled hierarchical attention-guided multiple instance learning for whole slide image classification. In *Proceedings of the Thirty-Second International Joint Conference on Artificial Intelligence*, pages 1587–1595, 2023. 3, 6

[37] Gang Xu, Zhigang Song, Zhuo Sun, Calvin Ku, Zhe Yang, Cancheng Liu, Shuhao Wang, Jianpeng Ma, and Wei Xu. Camel: A weakly supervised learning framework for histopathology image segmentation. In *Proceedings of the IEEE/CVF International Conference on computer vision*, pages 10682–10691, 2019. 2

[38] Jilan Xu, Junlin Hou, Yuejie Zhang, Rui Feng, Chunyang Ruan, Tao Zhang, and Weiguo Fan. Data-efficient histopathology image analysis with deformation representation learning. In *2020 IEEE International Conference on Bioinformatics and Biomedicine (BIBM)*, pages 857–864. IEEE, 2020. 3

[39] Pengshuai Yang, Zhiwei Hong, Xiaoxu Yin, Chengzhan Zhu, and Rui Jiang. Self-supervised visual representation learning for histopathological images. In *International Conference on Medical Image Computing and Computer-Assisted Intervention*, pages 47–57. Springer, 2021. 3

[40] Hongrun Zhang, Yanda Meng, Yitian Zhao, Yihong Qiao, Xiaoyun Yang, Sarah E Coupland, and Yalin Zheng. Dtfdmil: Double-tier feature distillation multiple instance learning for histopathology whole slide image classification. In *Proceedings of the IEEE/CVF conference on computer vision and pattern recognition*, pages 18802–18812, 2022. 2, 6

[41] Yuhao Zhang, Hang Jiang, Yasuhide Miura, Christopher D Manning, and Curtis P Langlotz. Contrastive learning of medical visual representations from paired images and text. In *Machine learning for healthcare conference*, pages 2–25. PMLR, 2022. 3

[42] Yuanpin Zhou and Yao Lu. Deep hierarchical multiple instance learning for whole slide image classification. In 2022

IEEE 19th international symposium on biomedical imaging
(ISBI), pages 1–4. IEEE, 2022. 3